

Electron capture and excitation in slow H^+ -He($2^{1,3}L$) collisions

C. H. Liu,¹ J. G. Wang,² and R. K. Janev^{3,4}¹*Institute of Modern Physics, Chinese Academy of Sciences, Lanzhou 730000, People's Republic of China*²*Institute of Applied Physics and Computational Mathematics, P.O. Box 8009-26, Beijing 100088, People's Republic of China*³*Macedonian Academy of Sciences and Arts, P.O. Box 428, 1000 Skopje, Macedonia*⁴*Institute of Energy and Climate Research-Plasma Physics, Forschungszentrum Jülich GmbH, Association EURATOM-FZJ, Trilateral Euregio Cluster, 52425 Jülich, Germany*

(Received 22 February 2012; revised manuscript received 4 April 2012; published 26 April 2012)

Dynamics of electron capture and excitation processes in collisions of H^+ with the excited He($2^{1,3}L_m$) atom ($L = S, P$) has been studied by using the full quantum-mechanical molecular orbital close-coupling (QMOCC) method with *ab initio* determined molecular states. 38 singlet and 37 triplet molecular states of the HeH⁺ system, that asymptotically correlate to the $n = 1-4$ projectile and target atomic states, have been included in the expansion basis. The shell- and state-selective electron capture and excitation cross sections have been calculated in the 0.01–6 keV/u energy range up to the $n = 4$ shell and their energy behavior discussed on the basis of identified reaction mechanisms.

DOI: 10.1103/PhysRevA.85.042719

PACS number(s): 34.70.+e, 34.20.-b

I. INTRODUCTION

The proton collision processes with ground state He($1s^2$) helium have been subject to numerous experimental and theoretical studies in the past (see, e.g., the collection of papers in Ref. [1], and references therein). Much less work has been done on these processes when the helium atom is in an excited state, He($1s, nl$). Such processes play, however, a very important role in the collisional-radiative kinetics of a fusion reactor divertor plasma (where helium will be the major intrinsic plasma impurity) and in the attenuation kinetics of plasma heating and diagnostic helium neutral beams (particularly when they contain a metastable fraction) [2,3]. There are no experimental studies of $H^+ + He(1s, nl)$ collision processes and the theoretical ones are only a few. The excitation of 2^1P and $3^1S, ^1P, ^1D$ states from the initial He(2^1S) state has been studied by using the atomic-orbital close-coupling method in the energy range of 6–150 keV/u [4]. In Ref. [5] calculations of excitation cross sections of triplet and singlet series from the initial $n = 2$ and $n = 3$ states up to $n = 5$ final states have been performed by employing the Glauber and Born approximations, while for ionization of He($n^{1,3}S$) and He($n^{1,3}P$) states with $n = 2-5$ cross sections have been performed within the continuum-distorted-wave-eikonal-initial-state approximation. The energy range covered in these calculations is 10–1000 keV/u. Finally, a molecular-orbital-type close-coupling method has been used in Ref. [6], with radial couplings calculated analytically by the asymptotic Landau-Herring method [7], to calculate the cross sections for electron capture and excitation from the $n^{1,3}L_m$ ($n = 2-4$, $L = S, P, D$) initial states to the final capture and excitation (deexcitation) states with $n = 1-4$. The rotational couplings and the electron momentum translational factors have not been included in these calculations, covering the energy range between 0.0021 and 8.8 keV/u.

In the present article we study the collision dynamics of electron capture and excitation processes,

$$H^+ + He(2^{1,3}L) \rightarrow H(nl) + He^+ \quad (1a)$$

$$\rightarrow H^+ + He(n^{1,3}L'), \quad (1b)$$

where $L = S, P$, $L' = S, P, D, F$ and $n = 1-4$ [$n = 1$ in Eq. (1b) denotes deexcitation]. We employ the full quantum-mechanical molecular-orbital close-coupling (QMOCC) method with *ab initio* determined molecular states and confine our study to the energy range 0.01–6 keV/u. The expansion basis contains 38 and 37 molecular states of singlet and triplet symmetries, respectively, all correlating to the $n = 1-4$ asymptotic states (see Sec. IV for details). Since no molecular orbital correlating to the $n = 5$ asymptotic states are included in the basis, our results for $n = 4$ in Eqs. (1a) and (1b) should be less reliable and we, therefore, present only the $n = 4$ shell capture and excitation cross sections.

The article is organized as follows. In the next section we briefly outline the QMOCC method used in the present study. In Sec. III we present the *ab initio* molecular structure data calculated by the multireference single- and double-excitation configuration interaction (MRD-CI) method [8,9]. In Sec. IV we present and discuss the calculated results, and in Sec. V we give our conclusions. Atomic units will be used throughout, unless explicitly indicated otherwise.

II. THEORETICAL METHOD

The description of the QMOCC method for an ion (atom)-atom collision system is given elsewhere (see, e.g., [10,11]), and here we present only a brief account of it. The QMOCC method treats both the electronic and nuclear motion in the system quantum mechanically and uses the adiabatic representation of electronic states. The collision dynamics involves solution of a set of second-order coupled differential equations which is solved by the log-derivative method of Johnson [12]. The transitions between adiabatic states are driven by radial and rotational (A^r and A^θ) couplings of the vector potential $\vec{A}(\vec{R})$, where \vec{R} is the internuclear distance vector. The electron momentum translational effects, important at higher collision velocities, can be accounted for within the QMOCC method by transforming the radial and rotational coupling matrix elements between the states ψ_K and ψ_L

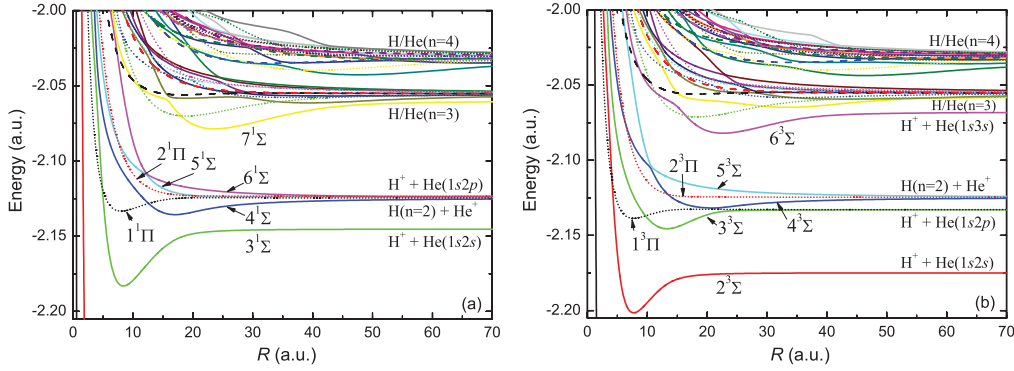


FIG. 1. (Color online) Potential energy curves of HeH^+ for (a) singlet states and (b) triplet states. The solid, dotted, and dashed lines represent the Σ , Π , and Δ states, respectively.

into Ref. [13]

$$\begin{aligned} \langle \psi_K | \partial / \partial R - (\varepsilon_K - \varepsilon_L) z^2 / 2R | \psi_L \rangle, \\ \langle \psi_K | iL_y + (\varepsilon_K - \varepsilon_L) zx | \psi_L \rangle, \end{aligned} \quad (2)$$

where ε_K and ε_L are the electronic energies of states ψ_K and ψ_L , and z^2 and zx are the components of the quadrupole moment tensor. This modification is similar in form to that resulting from the use of the common electron translation factor (ETF) approach in Ref. [14]. In order to avoid the numerical difficulties encountered in the integration of QMOCC equations based on the adiabatic representation of electronic states (related to the extremely sharp variation of some radial coupling matrix elements with R), it is convenient to make a unitary transformation [11,15] to a diabatic representation of electronic states. In this representation all the couplings have a smooth R behavior and the coupled second-order differential equations are solved with plane-wave boundary conditions at a large internuclear distance, R_{max} , to obtain the K matrix. Then the scattering matrix S is given by

$$S_J = [I + iK_J]^{-1} [I - iK_J], \quad (3)$$

where I is the identity matrix and J is the total angular momentum quantum number. The cross section for a transition from the initial channel α to the final channel β is expressed in terms of scattering matrix elements as

$$\sigma_{\alpha \rightarrow \beta} = \frac{\pi}{k_\alpha^2} \sum_J (2J+1) |\delta_{\alpha\beta} - S_{\alpha\beta}^J|^2, \quad (4)$$

where k_α is the initial momentum of center-of-mass motion.

III. MOLECULAR STRUCTURE CALCULATIONS

Ab initio CI calculations have been carried out for the singlet and triplet eigenstates of the HeH^+ system that asymptotically correlate to the H and He ($n = 1-4$) atomic states by using the MRD-CI package [8,9]. In the calculations of hydrogen, the correlation-consistent, polarization valence, quadruple- ζ -(cc-pVQZ)-type basis set [16] with a diffuse ($3s4p4d3f$) set was used. The cc-pVQZ-type basis set [16] with a diffuse ($4s5p5d5f$) basis was used also for the He atom. The final contracted basis set for the hydrogen atom was $(9s,7p,6d,4f)/[7s,7p,6d,4f]$ and that for the He

atom was $(11s,8p,7d,6f)/[8s,8p,7d,6f]$. A threshold of 10^{-8} hartree was used to select the configurations of HeH^+ at the internuclear distances between 0.2 and 100 a.u. The obtained electronic wave functions were then used to calculate the radial and rotational couplings by employing the finite-element differentiation and analytical approaches, respectively (see [17]).

The calculated adiabatic potential energy curves of molecular states of the HeH^+ ion correlating to the $n = 2-4$ H and He atomic states are shown in Figs. 1(a) and 1(b) for the singlet and triplet states, respectively, in the range $R = 0.2-70$ a.u. The lowest two singlet and one triplet states correlating to H($1s$) and He($1s^2$) are not shown in Fig. 1 because they are too far away from the initial He($1s, n = 2$) states.

It should be noted in Fig. 1 that some of the potential energy curves in the singlet and triplet system exert avoided crossings with the adjacent curves having the same symmetry. The most notable of them within the group of molecular states asymptotically correlating to the $n = 2$ group of H and He atomic states are those between the states $5^1\Sigma$ and $6^1\Sigma$ (at $R \approx 12$ a.u.) and $4^3\Sigma$ and $5^3\Sigma$ (at $R \approx 11$ a.u.). The figure also shows that within the groups of molecular states correlating to the $n = 3$ and $n = 4$ atomic H and He states, as well as between the states correlating to the $n = 2 - n = 3$ and $n = 3 - n = 4$ atomic H and He states, there are many such pairs of potential energy curves exerting avoided crossings.

In Fig. 2 we show the radial coupling matrix elements between the adjacent singlet [panel (a)] and triplet [panel (b)] states of the system that asymptotically correlate to the $n = 1, 2$ H and He atomic states. The sharply peaked radial couplings in these figures correspond to the states exerting an avoided crossing (see Fig. 1) where they are strongly coupled (Landau-Zener coupling). Besides the $5^1\Sigma-6^1\Sigma$ (at $R \approx 12$ a.u.) and $4^3\Sigma-5^3\Sigma$ (at $R \approx 11$ a.u.) couplings, it is also important to note in Fig. 2 the $6^1\Sigma-7^1\Sigma$ (at $R \approx 7$ a.u.), $5^3\Sigma-6^3\Sigma$ (at $R \approx 7.5$ a.u.), and $2^1\Pi-3^1\Pi$ (at $R \approx 4$ a.u. and $R \approx 1$ a.u., respectively) couplings that couple molecular states correlating to the $n = 2$ and $n = 3$ manifolds of atomic H and He states. The broad radial couplings between the molecular states converging to the asymptotic configurations He($1s, n = 2$) and H($n = 2$) observed at $R \approx 17$ a.u. for the $3^1\Sigma-4^1\Sigma$ states [cf. Fig. 2(a)], at $R \approx 13$ a.u. for the $2^3\Sigma-3^3\Sigma$ states, and at $R \approx 22$ a.u. for the $3^3\Sigma-4^3\Sigma$ states [cf. Fig. 2(b)], are due to the change of character of the electron wave function from an

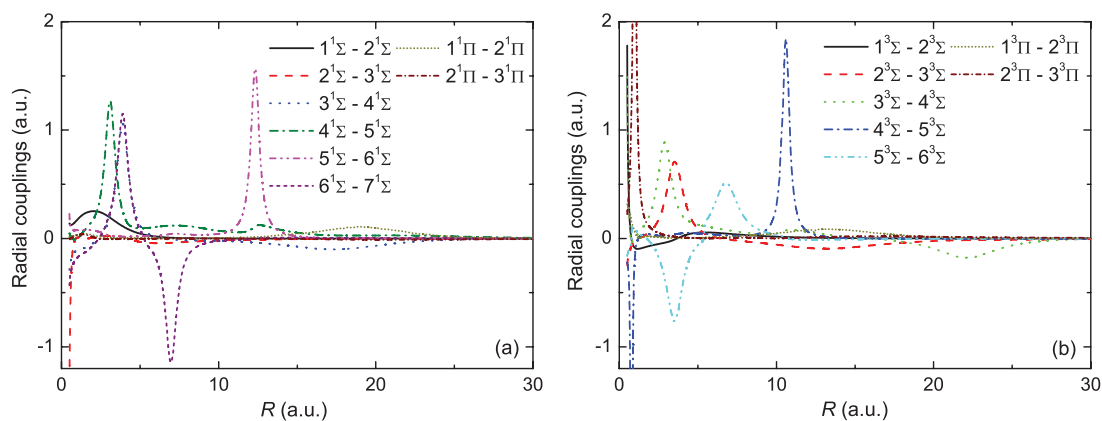


FIG. 2. (Color online) Radial coupling matrix elements between molecular states converging to $n = 1,2$ H and He atomic states (with exceptions of $6^1\Sigma-7^1\Sigma$, $5^3\Sigma-6^3\Sigma$ and $2^{1,3}\Pi-3^{1,3}\Pi$ couplings). (a) Singlet states; (b) triplet states.

atomic (localized) to a molecular (delocalized) one (Demkov coupling).

The radial Σ - Σ and Π - Π couplings between the adjacent molecular states of a given symmetry that asymptotically correlate to the $n = 3$ H and He atomic states are shown in Figs. 3(a) and 3(b) for the singlet and triplet states, respectively. For the sake of clarity, only the couplings in the range $R = 0.2-30$ a.u. are shown. In the region $R > 30$ a.u. there are several Demkov-type couplings between quasidegenerate states that asymptotically converge to the $\text{He}^+ + \text{H}(n = 3)$ and $\text{H}^+ + \text{He}(3l)$ configurations [for instance, the $7^1\Sigma-8^1\Sigma$ (at $R \sim 45$ a.u.), $6^3\Sigma-7^3\Sigma$ (at $R \sim 35$ a.u.), $7^3\Sigma-8^3\Sigma$ (at $R \sim 56$ a.u.), $3^1\Pi-4^1\Pi$ (at $R \sim 50$ a.u.), and $3^3\Pi-4^3\Pi$ (at $R \sim 35$ a.u.); see Fig. 1]. Also not shown in Fig. 3 are the radial couplings that couple the considered molecular states with the group of molecular states that asymptotically converge to the $n = 4$ H and He atomic states. From Fig. 1 one can see that in the region $R < 30$ a.u. there are many such couplings. It can be also seen from Figs. 1 and 3 that within the $n = 3$ and $n = 4$ groups of molecular states, two consecutive states of the same symmetry can be strongly coupled more than once when the internuclear separation changes.

We should note that the radial couplings between molecular states of a given symmetry, particularly the ones that take

place at large internuclear distances, play a major role in the excitation and electron capture dynamics.

In Fig. 4 we show the rotational couplings between the Σ and Π molecular states of singlet [panel (a)] and triplet [panel (b)] symmetry that asymptotically converge to $n = 2$ H and He atomic states. We should note the particularly large values of rotational couplings between the states converging to the asymptotic configurations $\text{H}^+ + \text{He}(1s, 2p\sigma, \pi)$ and $\text{He}^+ + \text{H}(2p\sigma, \pi)$.

The rotational couplings of $4-7^1\Sigma$ and $3-6^3\Sigma$ molecular states with the $^1\Pi$ and $^3\Pi$ states that asymptotically converge to the $3p\pi$ and $3d\pi$ H and He states are shown in Figs. 5(a) and 5(b), respectively. It should be noted that all Σ states in these couplings, except $7^1\Sigma$ and $6^3\Sigma$, asymptotically converge to the $n = 2$ H and He atomic σ states. Therefore, together with earlier mentioned $6^1\Sigma-7^1\Sigma$, $5^3\Sigma-6^3\Sigma$, and $2^{1,3}\Pi-3^{1,3}\Pi$ radial couplings, these rotational couplings couple the molecular states that asymptotically converge to $n = 2$ H and He atomic states with the group of molecular states that converge to $n = 3$ H and He atomic states. The rotational couplings between the states from the $n = 3$ group of molecular states with those that asymptotically converge to the $n = 4$ H and He atomic states are not shown in Fig. 5 for the sake of clarity.

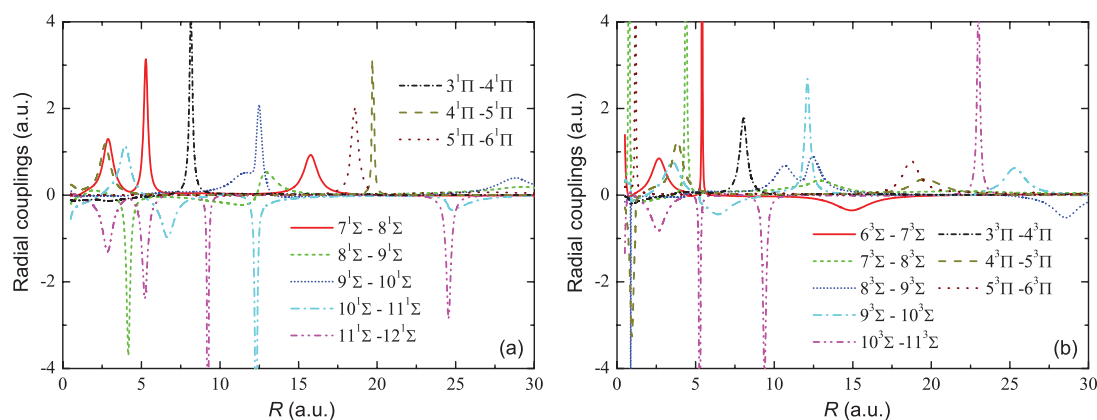


FIG. 3. (Color online) Radial coupling matrix elements between molecular states converging to $n = 3$ H and He atomic states. (a) Singlet states; (b) triplet states.

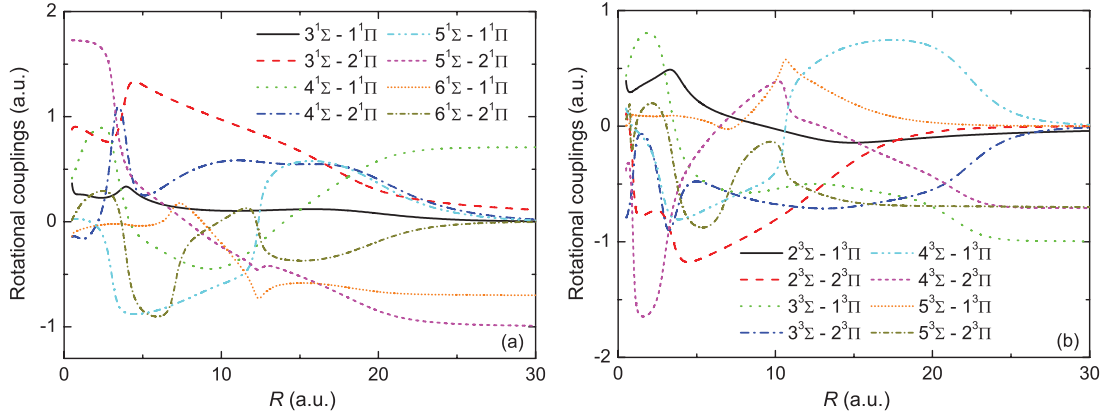


FIG. 4. (Color online) Rotational couplings between the Σ and Π molecular states converging to $n = 2$ H and He atomic states. (a) Singlet states; (b) triplet states.

From the point of view of the collision dynamics it is important to note that the singlet and triplet molecular states are not mutually coupled. Therefore, the coupled equations for the transitions between molecular states of a given spin symmetry are solved separately. Furthermore, the π ($m = \pm 1$) and δ ($m = \pm 2$) molecular orbitals have a well-defined symmetry with respect to the collision plane: the states π^+ and δ^+ , which lie on the collision plane, are symmetric, while the states π^- and δ^- , which are perpendicular to the collision plane, are antisymmetric. These two types of states (having the same energy) are not mutually coupled, which results in an additional decoupling of QMOCC equations with respect to this symmetry.

It is also important to note that the molecular states describing the capture channels at large internuclear distances go over to the hydrogen Stark states (produced by the field of the He^+ ion). In order to obtain the capture results in the angular momentum representation of atomic states, the corresponding Stark states have to be projected onto angular momentum states. The correlation between the molecular and atomic H and He states having principal quantum numbers $n = 1-3$ for asymptotically large internuclear distances is given in Table I, in which we also show the linear combinations of H atom angular momentum states from which the relevant Stark states are built.

IV. CROSS-SECTION RESULTS AND DISCUSSIONS

As mentioned in the Introduction, the cross sections of electron capture and excitation processes (1a) and (1b) have been calculated in the present work by the QMOCC method in the energy range 0.01–6 keV/u. In the expansion basis we have included all Σ and Π states correlating asymptotically to the $n = 1-4$ H and He atomic states, as well as two Δ states from the $n = 3$ manifold. In total, 34 singlet and 33 triplet molecular states were included in the basis for the initial $\text{He}(1s, 2s)$ and $\text{He}(1s, 2p\pi^+)$ states. We have checked that these calculations would differ very little with those that include all Σ , Π , and Δ states asymptotically to the $n = 1-4$ H and He atomic states (i.e., 38 singlet and 37 triplet states). For the initial $\text{He}(1s, 2p\pi^-)$ state, all Π and Δ states are included; that is, 18 singlet and 18 triplet states. We note that the QMOCC equations for each spin system of states are further decoupled with respect to the $+/-$ symmetry of the π and δ states mentioned in the preceding section.

The initial molecular configurations involved in the processes (1a) and (1b) are the $\text{H}^+ + \text{He}(2s)$, $\text{H}^+ + \text{He}(2p\sigma)$, and $\text{H}^+ + \text{He}(2p\pi^\pm)$ that generate the singlet $3^1\Sigma, 5^1\Sigma, 2^1\Pi^\pm$ and triplet $2^3\Sigma, 3^3\Sigma, 1^3\Pi^\pm$ molecular states, respectively. As mentioned earlier, the Π^\pm have the same energy (same potential energy curve in Fig. 1). During the approaching

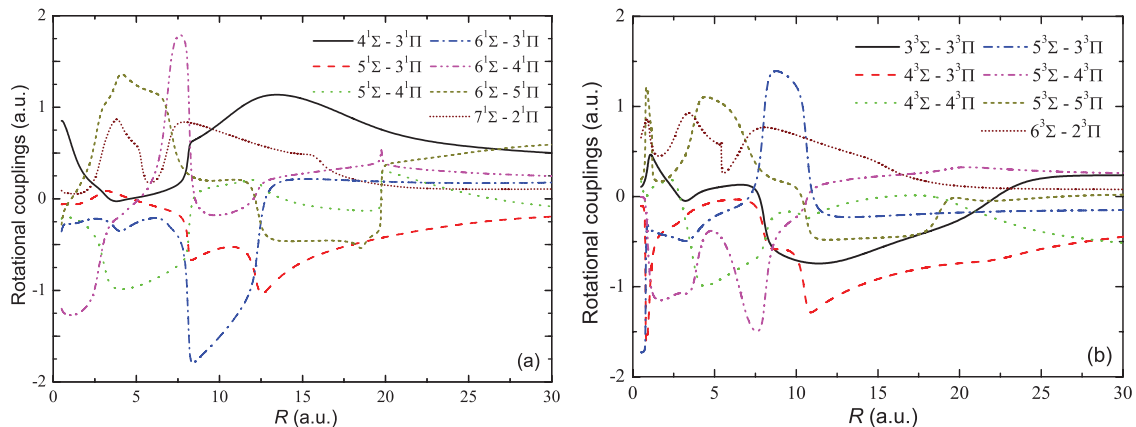


FIG. 5. (Color online) Rotational couplings between the Σ and Π molecular states correlating to the $n = 2$ states with $n = 3$ states. (a) Singlet states; (b) triplet states.

TABLE I. Correlation between the molecular and atomic H and He $n = 1-3$ states at asymptotically large internuclear separations.

Molecular state	Asymptotic states	Linear combinations of H states
$1^1\Sigma$	$H^+ + He(1s^2)$	
$2^1\Sigma, 1^3\Sigma$	$H(1s) + He^+(1s)$	
$3^1\Sigma, 2^3\Sigma$	$H^+ + He(1s2s)$	
$4^1\Sigma, 4^3\Sigma$	$H(2\sigma_1) + He^+(1s)$	$ 2\sigma_1\rangle = (2s\rangle - 2p\sigma\rangle)/\sqrt{2}$
$6^1\Sigma, 5^3\Sigma$	$H(2\sigma_2) + He^+(1s)$	$ 2\sigma_2\rangle = (2s\rangle + 2p\sigma\rangle)/\sqrt{2}$
$5^1\Sigma, 3^3\Sigma$	$H^+ + He(1s2p\sigma)$	
$7^1\Sigma, 6^3\Sigma$	$H^+ + He(1s3s)$	
$8^1\Sigma, 8^3\Sigma$	$H(3\sigma_1) + He^+(1s)$	$ 3\sigma_1\rangle = (\sqrt{2} 3s\rangle - \sqrt{3} 3p\sigma\rangle + 3d\sigma\rangle)/\sqrt{6}$
$9^1\Sigma, 10^3\Sigma$	$H^+ + He(1s3d\sigma)$	
$10^1\Sigma, 9^3\Sigma$	$H(3\sigma_2) + He^+(1s)$	$ 3\sigma_2\rangle = (\sqrt{2} 3s\rangle - 2 3d\sigma\rangle)/\sqrt{6}$
$11^1\Sigma, 7^3\Sigma$	$H^+ + He(1s3p\sigma)$	
$12^1\Sigma, 11^3\Sigma$	$H(3\sigma_3) + He^+(1s)$	$ 3\sigma_3\rangle = (\sqrt{2} 3s\rangle + \sqrt{3} 3p\sigma\rangle + 3d\sigma\rangle)/\sqrt{6}$
$1^1\Pi, 2^3\Pi$	$H(2p\pi) + He^+(1s)$	
$2^1\Pi, 1^3\Pi$	$H^+ + He(1s2p\pi)$	
$3^1\Pi, 4^3\Pi$	$H(3\pi_1) + He^+(1s)$	$ 3\pi_1\rangle = (3p\pi\rangle - 3d\pi\rangle)/\sqrt{2}$
$4^1\Pi, 5^3\Pi$	$H^+ + He(1s3d\pi)$	
$5^1\Pi, 6^3\Pi$	$H(3\pi_2) + He^+(1s)$	$ 3\pi_2\rangle = (3p\pi\rangle + 3d\pi\rangle)/\sqrt{2}$
$6^1\Pi, 3^3\Pi$	$H^+ + He(1s3p\pi)$	
$1^1\Delta, 1^3\Delta$	$H^+ + He(1s3d\delta)$	
$2^1\Delta, 2^3\Delta$	$H(3d\delta) + He^+(1s)$	

stage of the collision, the system from any of these initial molecular states evolves along its potential energy curve and undergoes transitions at each of the radial and rotational strong-coupling regions. At each of these strong-coupling regions the probability flux undergoes branching. In the region of small internuclear distances the probability flux carried out by the populated molecular states correlating with the $n = 2$ group of asymptotic states is transferred (mainly by rotational coupling) to the group of molecular states converging to the asymptotic $n = 3$ H and He manifolds. During the receding stage of the collision, the radial and rotational couplings between molecular states within the group of states converging

to the $n = 3$ asymptotic H and He manifolds, as well as the coupling of these states with those converging to the $n = 4$ asymptotic H and He manifold, determine the populations of exit reaction channels with $n = 3$ and $n = 4$. For simplicity, we represent the collision dynamics within the singlet and triplet system of states by the schematic correlation diagrams in Figs. 6(a) and 6(b), respectively, in which the most important couplings are indicated. The relative weak couplings between not adjacent states are not included in this figure. The rotational couplings are generally active at small internuclear distances, except those between the asymptotically degenerate states.

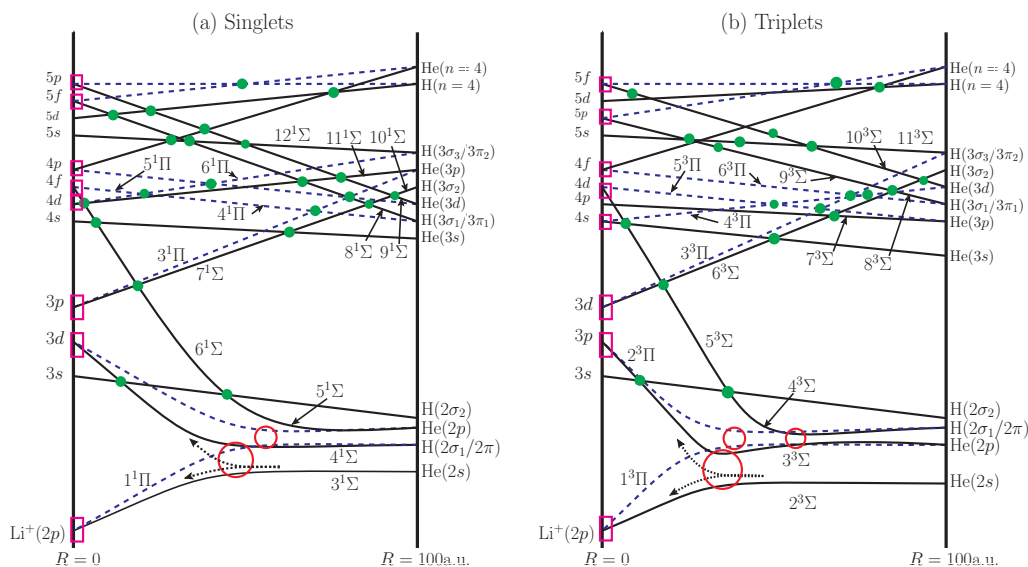


FIG. 6. (Color online) Schematic correlation diagram of singlet and triplet energies of the HeH^+ system. The open circles represent the Demkov couplings, the solid circles represent the Landau-Zener pseudocrossings, and the open squares represent the rotational couplings.

We note that the cross sections for the initial He($2^{1,3}P\pi$) states can be expressed as

$$\sigma_{\pi} = \frac{1}{2}[\sigma_{\pi+} + \sigma_{\pi-}], \quad (5)$$

while the total cross sections for the initial He($2^{1,3}P$) states are weighted averages of the cross sections for the initial He($2^{1,3}P\sigma$) and He($2^{1,3}P\pi$) states, i.e.,

$$\sigma_p = \frac{1}{3}[\sigma_{\sigma} + 2\sigma_{\pi}] = \frac{1}{3}[\sigma_{\sigma} + \sigma_{\pi+} + \sigma_{\pi-}]. \quad (6)$$

A. Electron capture cross sections

1. He($2^{1,3}S$) initial states

In Fig. 7 we show our QMOCC results for electron capture cross sections from the initial 2^1S and 2^3S states of He to the $n = 1-4$ shells of H. The figure shows that with increasing n by one, the cross sections for capture to $n = 2-4$ shells decrease by about an order of magnitude for both 2^1S and 2^3S initial states of He. Another remarkable feature of $n = 2-4$ capture cross sections is the much faster decrease with energy of the cross sections from the He(2^3S) initial state in the low energy region than the corresponding ones when the initial state is He(2^1S). A rough understanding of the magnitude and energy behavior of these capture cross sections, as well as that for capture to the $1s$ state, can be gained from the Massey adiabatic criterion and asymptotic reaction energy defects. A more detailed picture about the excitation and capture dynamics, however, can be obtained by analyzing the potential energy curves and the couplings involved in the evolution of the system along various reaction paths leading to population of each H(n) shell, or just analyzing that evolution with the help of the schematic diagrams in Fig. 6.

In the case of the He(2^1S) initial state, the collision system in its approaching stage evolves along the $3^1\Sigma$ molecular state which at $R \approx 17$ a.u. is coupled by a Demkov coupling with the $4^1\Sigma$ state [cf. Figs. 1(a) and 2(a)]. During the further evolution of the system toward the united atom region, it evolves (with well-defined probabilities) along both the $3^1\Sigma$ and $4^1\Sigma$ states, the latter of which is also coupled with the $5^1\Sigma$ state at $R \approx 3$ a.u. by a Landau-Zener coupling [see Fig. 2(a)]. At small internuclear distances, the $3^1\Sigma$, $4^1\Sigma$, and $5^1\Sigma$ states are rotationally coupled [see Fig. 3(a)] with the $1^1\Pi$ and $2^1\Pi$

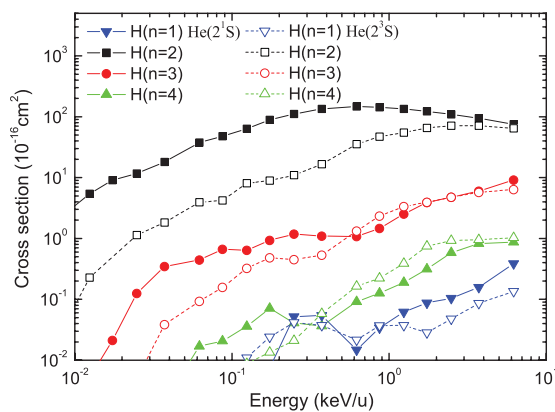


FIG. 7. (Color online) Cross sections for electron capture to H($n = 1-4$) shells from the He($2^{1,3}S$) initial states.

states (the later correlating to the $2p\pi$ H and He atomic states), while the $4^1\Sigma$ and $5^1\Sigma$ states are rotationally coupled also [see Fig. 5(a)] with the $3^1\Pi$ and $4^1\Pi$ states, respectively (the latter correlating to the $3p\pi$ and $3d\pi$ H and He atomic states). In the receding stage of the collision, the populated $3, 4, 5^1\Sigma$ and $1, 2^1\Pi$ states undergo the radial Landau-Zener $4^1\Sigma-5^1\Sigma$, $5^1\Sigma-6^1\Sigma$ (at $R \approx 12$ a.u.), $2^1\Pi-3^1\Pi$ (at $R \approx 4$ a.u.) and Demkov $3^1\Sigma-4^1\Sigma$ and $1^1\Pi-2^1\Pi$ (at $R \approx 18$ a.u.) couplings. In the separated atom limit, the molecular states $4^1\Sigma$ and $6^1\Sigma$ populate the H($2s$) and H($2p\sigma$) capture states (of which they are of linear combination), while the state $1^1\Pi$ state populates the H($2p\pi$) capture state (see Table I). [The states $5^1\Sigma$ and $2^1\Pi$ populate the He($2p\sigma$) and He($2p\pi$) excited states.] From Fig. 5(a) we see that the $2^1\Pi$ state is rotationally coupled with the $7^1\Sigma$ state, which is at $R \approx 16$ a.u. radially coupled with the $8^1\Sigma$ state (cf. Fig. 3). The $3^1\Pi, 4^1\Pi$ states are rotationally coupled with the $6^1\Sigma$ state, which in the receding stage of the collision initiates the $6^1\Sigma-7^1\Sigma$ (at $R \approx 7.5$ a.u.) and $7^1\Sigma-8^1\Sigma$ series of Landau-Zener couplings (see Fig. 3). The $3^1\Pi, 4^1\Pi$ states also initiate a series of Landau-Zener couplings: $3^1\Pi-4^1\Pi$ (at $R \approx 7$ a.u.), $4^1\Pi-5^1\Pi$ (at $R \approx 19.5$ a.u.) and $4^1\Pi-5^1\Pi$ (at $R \approx 3$ a.u.), $5^1\Pi-6^1\Pi$ (at $R \approx 18$ a.u.) [see Fig. 3(a)]. As mentioned in the preceding section, at internuclear distances above 30 a.u. the states of $^1\Sigma$ and $^1\Pi$ symmetry are coupled with other states of the same symmetry by radial Demkov couplings.

The group of molecular states that asymptotically correlate to the $n = 4$ H and He atomic states is initially populated mainly by rotational couplings with the group of states converging to the $n = 3$ H and He atomic states at small internuclear distances [see Fig. 6(a)]. The radial couplings within this group of states that take place at larger internuclear separations define the final distribution of the population of $n = 4$ H and He atomic states.

The difference in the magnitude of cross sections for capture to $n = 2-4$ states is due to the fact that from the multitude of states along which the system evolves in the incoming stage of the collisions, only a small number are coupled with the states from the group of molecular states that converge to $n = 3$ H and He atomic states. Even a smaller number of states of this latter group are coupled with the group of states that asymptotically correlate with the $n = 4$ H and He atomic states [see Fig. 6(a)]. It should be also kept in mind that each consecutive coupling of the probability flux is reduced. These arguments obviously hold also for the relative magnitude of excitation cross sections for $2p$, $n = 3$ and $n = 4$ singlet states of He discussed later in this section.

In the case when the initial state in the collision is He(2^3S) the collision dynamics is somewhat different from that of the He(2^1S) initial state [compare Figs. 6(a) and 6(b)]. In the approaching stage of the collision, the $2^3\Sigma$ initial molecular state exerts a Demkov coupling with the $3^3\Sigma$ state (at $R \approx 13$ a.u.), which asymptotically correlates to the He($2p\sigma$) state (i.e., it is not a capture state). Only in the receding stage of the collision is the $3^3\Sigma$ state coupled with the $4^3\Sigma$ state by a weak Landau-Zener coupling [at $R \approx 2.5$ a.u.; see Fig. 2(b)], and later on these two states interact again (at $R \approx 22$ a.u.) by a Demkov coupling [cf. Fig. 2(b)]. The $4^3\Sigma$ molecular state at asymptotically large internuclear distances represents a linear combination of $2s$ and $2p\sigma$ H states (see Table I). The $4^3\Sigma$ state undergoes a strong Landau-Zener coupling with the state

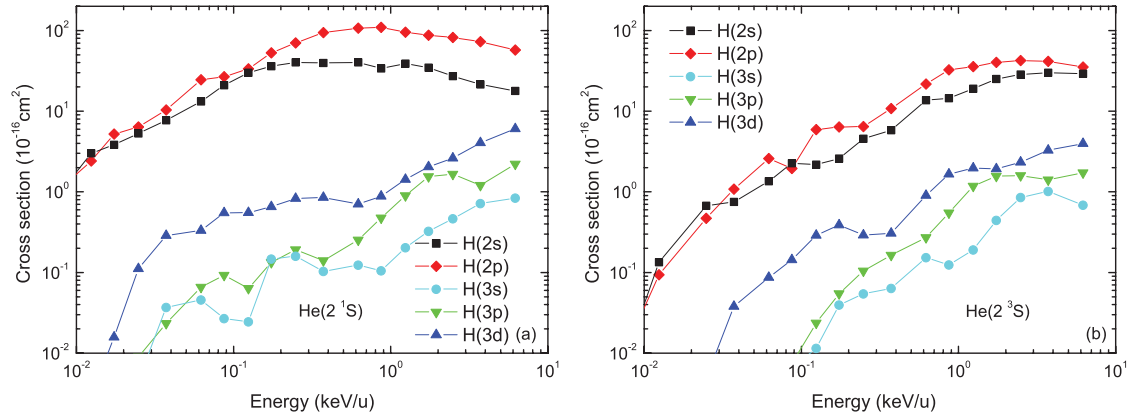


FIG. 8. (Color online) Cross sections for electron capture to nl states of the H atom from the $\text{He}(2^{1,3}S)$ initial states. (a) Singlet states; (b) triplet states.

$5^3\Sigma$ [at $R \approx 10.5$ a.u.; see Fig. 2(b)], which asymptotically represents also a linear combination of $2s$ and $2p\sigma$ H states. Finally, the $2,3,4^3\Sigma-1,2^3\Pi$ rotational couplings [cf. Fig. 4(b)] populate the $1^3\Pi$ and $2^3\Pi$ states, which at $R \approx 13.5$ a.u. are mutually coupled by a Demkov coupling ([cf. Figs. 1(b) and 2(b)]. The state $2^3\Pi$ asymptotically correlates with the $2p\pi$ H state. The main couplings that promote the probability flux from the group of molecular states converging to $n = 2$ H and He states to the groups of molecular states converging to the $n = 3, 4$ H and He states are the radial $5^3\Sigma-6^3\Sigma$ and $2^3\Pi-3^3\Pi$ [see Fig. 3(b)] and rotational $2^3\Pi-6^3\Sigma$, $3^3\Sigma-3^3\Pi$, and $4^3\Sigma-3,4^3\Pi$ couplings [see Fig. 5(b)].

The differences in the magnitude and energy behavior of the n -shell capture cross sections observed in Fig. 7 for the $\text{He}(2^1S)$ and $\text{He}(2^3S)$ initial states originate from the differences in the reaction paths leading to the final H n manifolds of states, as well as from the differences in the positions and strengths of corresponding couplings [compare Figs. 2(a)–5(a) with Figs. 2(b)–5(b), respectively]. The most important coupling that in both cases defines the probability flux going to the inelastic channels is the one experienced first by the system in the approaching stage of the collision. In the case of $\text{He}(2^1S)$ and $\text{He}(2^3S)$ initial states, these are the $3^1\Sigma-4^1\Sigma$ (at $R \approx 17$ a.u.) and $2^3\Sigma-3^3\Sigma$ (at $R \approx 13$ a.u.) Demkov couplings, respectively. From Figs. 1(a) and 1(b) we see that the energy separation between the $3^1\Sigma$ and $4^1\Sigma$ states in the coupling region (≈ 0.570 eV) is considerably smaller than that between the $2^3\Sigma$ and $3^3\Sigma$ states (≈ 1.366 eV). This difference (of ≈ 0.796 eV) in the energy separations of the two pairs of coupled states does not significantly affect the corresponding transition probability at high collision velocities, when the strong-coupling R regions are passed quickly, but it does so at the low collision velocities when the system passes these regions slowly (adiabatically). The large energy separation of coupled states increases the adiabaticity of the collision and thereby reduces the transition probability. Figure 1 indicates that the described adiabatic effect in the $2^3\Sigma-3^3\Sigma$ coupling is propagated in the remaining part of the collision dynamics and is manifested in the energy behavior of all $n = 2-4$ capture cross sections [faster decrease with energy of the cross sections for the $\text{He}(2^3S)$ initial state with respect to those for the $\text{He}(2^1S)$ initial state]. It is also seen

from Fig. 7 that in the case of capture to $n = 3$ and $n = 4$ shells the adiabatic effect becomes apparent at energies below ~ 0.5 and ~ 0.3 keV/u, respectively, while for the higher energies the capture to $n = 3, 4$ shells is affected also by the other couplings involved in the population of these shells. Finally, we note that the electron capture to the H($1s$) state is governed by Demkov-type $3^1\Sigma-2^1\Sigma$ and $2^3\Sigma-1^3\Sigma$ couplings which are weak and appear at small internuclear distances (see Fig. 2) due to the large energy separations (≈ 9.634 and ≈ 8.838 eV, respectively) in the interaction region. Finally, it should be noted that in the population of $n = 2-4$ states in the case of the $\text{He}(2^3S)$ initial state an additional coupling in the capture dynamics is involved [with respect to that for the initial $\text{He}(2^1S)$ state] in order to reach the final capture channels (namely, the $3^3\Sigma-4^3\Sigma$ coupling). This leads to an additional reduction of the $n = 2-4$ capture cross sections in the case of the $\text{He}(2^3S)$ initial state.

The electron capture dynamics reveals itself in more detail in the nl -capture cross sections. In Figs. 8(a) and 8(b) we show the cross sections for electron capture to H($2l$) and H($3l$) states from the $\text{He}(2^1S)$ and $\text{He}(2^3S)$ initial states, respectively. We observe that in the case of the $\text{He}(2^3S)$ initial state the populations of $2s$ and $2p$ H states are close to each other, whereas in the case of the $\text{He}(2^1S)$ initial state the population of the $2p$ state is considerably larger than that of the $2s$ state for energies higher than ~ 0.2 keV/u. The closeness of $2s$ and $2p$ cross sections in the case of the $\text{He}(2^3S)$ initial state is related to the fact that the $2s$ and $2p\sigma$ states are populated from the same molecular states, $4^3\Sigma$ and $5^3\Sigma$ (the contribution of the latter being small), and that the Demkov $1^3\Pi-2^3\Pi$ coupling (at $R \approx 13.5$ a.u.) is relatively weak [due to the sizable energy separation of these two states in the coupling region; see Figs. 1(b) and 2(b)] to provide a significant population of the $2p\pi$ H state. In contrast to this situation, the $1^1\Pi$ and $2^1\Pi$ states are energetically almost degenerate for $R \geq 20$ a.u. (their energy difference is only 0.032 eV) and their radial coupling at $R \approx 18$ a.u. ensures a significant $2p\pi$ contribution to the $2p$ H state at energies above 0.2 keV/u.

Among the $3l$ cross sections, the largest one for both initial $\text{He}(2^{1,3}S)$ states is that for capture to H($3d$) and the smallest one is that for capture to H($3s$) in the entire energy range investigated. This is because the largest number of channels

contribute to $H(3d)$. The $3l$ cross sections in both cases exhibit similar oscillatory structures. These structures are due to the fact that the radial couplings involved in the population of $3l$ capture states operate at different internuclear distances (see Figs. 2 and 3) and contribute significantly to the $3l$ capture cross sections at different energies. The smaller magnitudes of $2l$ and $3l$ cross sections for the initial triplet states with respect to those for the singlet one and their faster decrease with decreasing the energy are a consequence of previously discussed weak $2^3\Sigma$ - $3^3\Sigma$ coupling.

2. $\text{He}(2^{1,3}P)$ initial states

In the $\text{H}^+ + \text{He}(2p)$ collision system, the components $\text{He}(2p\sigma)$ and $\text{He}(2p\pi^\pm)$ of the $\text{He}(2p)$ state generate, respectively, the $5^1\Sigma$ and $2^1\Pi$ molecular states in the $\text{He}(2^1P)$ case and the $3^3\Sigma$ and $1^3\Pi$ molecular states in the $\text{He}(2^3P)$ case.

In the case of the singlet $\text{He}(2p\sigma)$ initial state, the evolution of the system along the $5^1\Sigma$ molecular state in the approaching stage of the collision involves the Landau-Zener $5^1\Sigma$ - $6^1\Sigma$ (at $R \approx 12$ a.u.) and $6^1\Sigma$ - $7^1\Sigma$ (at $R \approx 7$ a.u.) couplings and their rotational couplings of these states with the $^1\Pi$ states at small internuclear distances [cf. Fig. 6(a)]. In the receding stage of the collision, the radial couplings between the H and He ($n = 2$) states affect the population of the states converging to $n = 2$ H and He atomic states, while the series of radial couplings between $n = 2$ and $n = 3$ states and couplings between $n = 3$ states affect the populations of the states converging to $n = 3$ H and He atomic states [see Fig. 6(a) and Sec. IV A1].

In the case of the singlet $\text{He}(2p\pi^+)$ initial state, the collision system in the approaching stage evolves along the $2^1\Pi$ molecular state, which at $R \approx 18$ a.u. interacts with the $1^1\Pi$ state by a Demkov coupling and at $R \approx 4$ a.u. interacts with the $3^1\Pi$ state by a Landau-Zener coupling. At small internuclear distances the rotational couplings populate the $n = 2^1\Sigma$ states and some of the $n = 3^1\Sigma$ and $^1\Delta$ states). In the receding stage of the collision, the radial couplings are those that determine the population of the states converging to $n = 2, 3$ H and He atomic states [see Fig. 6(a)]. In the asymptotic region, the $4^1\Sigma$ and $6^1\Sigma$ molecular states both converge to a linear combination of $2s$ and $2p$ H states, while the $1^1\Pi$ molecular state converges to the $2p$ H state.

For the initial singlet $\text{He}(2p\pi^-)$ state, a similar analysis can be made but the $^1\Sigma$ states are not included.

In the case of triplet $\text{He}(2p\sigma, \pi^\pm)$ initial states, the collision dynamics are similar to those for the corresponding singlet states, but the initial $\text{He}(2p)$ states are lower than those of $H(n = 2)$ at large internuclear distances, and an additional radial coupling, $3^3\Sigma$ - $4^3\Sigma$, is involved in the collision [see Fig. 6(b)].

The cross sections for electron capture to the $n = 1-4$ H shells for the initial $\text{He}(2^{1,3}P)$ states, obtained by averaging the computed cross sections for the specific values of magnetic substates, Eq. (6), are shown in Fig. 9. The cross sections for capture to $1s$ and $n = 2-4$ shells for the two initial states are remarkably close to each other, except for the $n = 3$ case where the cross section for the triplet initial state is smaller than that for the singlet initial state for energies below 0.03 keV/u and above 0.3 keV/u. This is in contrast with the n -shell capture cross sections for capture from $\text{He}(2^{1,3}S)$ initial states

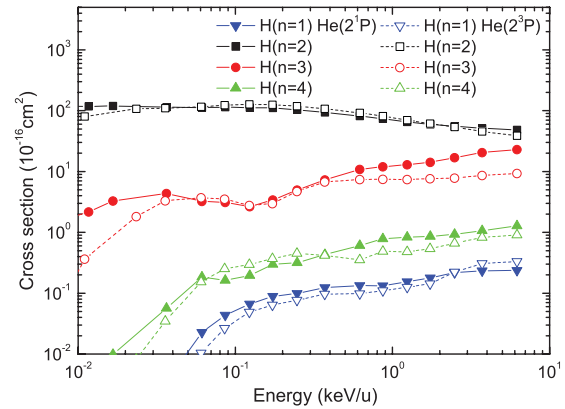


FIG. 9. (Color online) Cross sections for electron capture to $H(n)$ states from the $\text{He}(2^{1,3}P)$ initial states.

(compare Figs. 7 and 9). The proximity of the corresponding $n = 1-4$ shell capture cross sections is an obvious consequence of the similarity of the above described collision dynamics for the two initial states of He. This is also true for the capture to the $H(1s)$ capture state which in the case of the $\text{He}(2^1P)$ initial state is populated mainly by the $2^1\Pi$ - $2^1\Sigma$ rotational coupling, while in the case of the $\text{He}(2^3P)$ initial state it is populated mainly by the $1^3\Pi$ - $1^3\Sigma$ rotational coupling. It should be noted that the energy dependence of n -shell cross sections for $\text{He}(2^{1,3}P)$ initial states (Fig. 9), particularly for $n = 2$ and $n = 3$, is significantly different from that for $\text{He}(2^{1,3}S)$ initial states (Fig. 7).

The capture dynamics is better manifested in the cross sections for electron capture to $H(nl)$ ($n = 2, 3$) shown in Figs. 10(a) and 10(b) for the $\text{He}(2^1P)$ and $\text{He}(2^3P)$ initial states, respectively. There are significant differences in the magnitudes and energy behavior of the $2p$ and $2s$ capture cross sections for the two initial states. We recall that the $H(2s)$ state is populated by the $4^1\Sigma$ and $6^1\Sigma$ exit molecular channels in the case of the singlet initial state and by the $4^3\Sigma$ and $5^3\Sigma$ exit channels in the triplet case. These channels also populate the $H(2p)$ state, but the main contribution to the population of this state comes from the $1^1\Pi$ and $2^3\Pi$ states in the singlet and triplet cases, respectively (see Table I). In both cases, the long distant Demkov $1^{1,3}\Pi$ - $2^{1,3}\Pi$ couplings play a decisive role in the population of the $2p$ state when the initial states are $\text{He}(2^{1,3}P\pi)$ as they take place first in the approaching stage of the collision. Due to the small energy difference of the $1^1\Pi$ and $2^1\Pi$ states in the strong-coupling region (≈ 0.032 eV) and the large internuclear distance at which $1^1\Pi$ - $2^1\Pi$ coupling takes place ($R \sim 18$ a.u.), the $2p$ capture cross section for the $\text{He}(2^1P)$ initial state attains its maximum at very low energies (~ 0.01 keV/u). In the case of the $\text{He}(2^3P)$ initial state, the energy difference of $1^3\Pi$ and $2^3\Pi$ states in the strong-coupling region ($R \sim 13.5$ a.u.) is much larger (≈ 0.223 eV) and the maximum of the $2p$ capture cross section appears at about 0.3 keV/u.

The differences in the energy behavior of the cross sections for capture to the $H(2s)$ state for the $\text{He}(2^1P)$ and $\text{He}(2^3P)$ initial states result mainly from the differences in the couplings operating during the approaching stage of the collision (see discussions above). In the case of the $\text{He}(2^1P)$ initial state, the only molecular state populated in the approaching stage from

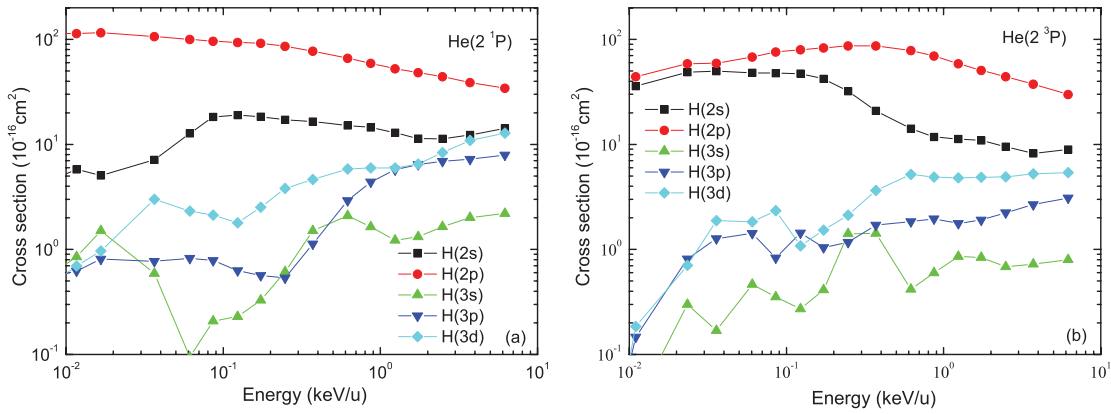


FIG. 10. (Color online) Cross sections for electron capture to nl states of H from the $\text{He}(2\ ^1P)$ (a) and $\text{He}(2\ ^3P)$ (b) initial states.

the initial molecular $5\ ^1\Sigma$ state, that in the receding stage of the collision populates the $\text{H}(2s)$ capture state, is the $6\ ^1\Sigma$ state. In both the approaching and receding stage, this state is depopulated by the $6\ ^1\Sigma$ - $7\ ^1\Sigma$ coupling (at $R \approx 7$ a.u.), and in the receding stage it is further depopulated by the $6\ ^1\Sigma$ - $5\ ^1\Sigma$ coupling (at $R \approx 12$ a.u.). These successive couplings account for the relatively small magnitude of the $2s$ capture cross section at low energies observed in Fig. 10(a). In the case of the $\text{He}(2\ ^3P)$ initial state, the initial molecular $3\ ^3\Sigma$ state in the approaching stage of the collision initiates the series of $3\ ^3\Sigma$ - $4\ ^3\Sigma$ - $5\ ^3\Sigma$ radial couplings. In the receding stage of the collision, both $4\ ^3\Sigma$ and

$5\ ^3\Sigma$ molecular states populate the $\text{H}(2s)$ capture state, which makes the $2s$ capture cross section in Fig. 10(b) large at low collision energies.

The population of $\text{H}(3l)$ capture states for both the $\text{He}(2\ ^1P)$ and $\text{He}(2\ ^3P)$ initial states is determined by the coupling dynamics within the $n = 3$ group of molecular states populated mainly by the rotational couplings at small internuclear distances. The structures in the energy behavior of the $3l$ capture cross sections observed in Figs. 10(a) and 10(b) result from different reaction paths contributing to the same final capture state.

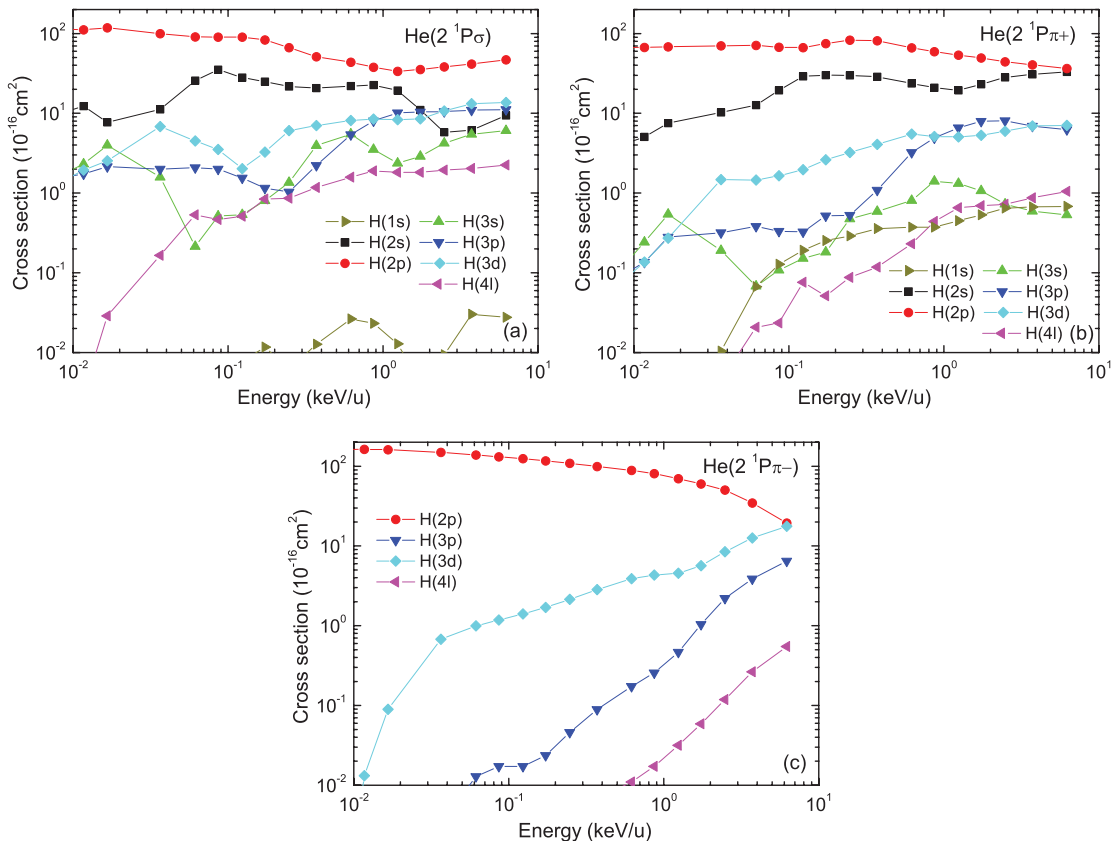


FIG. 11. (Color online) Cross sections for electron capture to $\text{H}(nl)$ states from the $\text{He}(2\ ^1P\sigma)$ (a), $\text{He}(2\ ^1P\pi^+)$ (b), and $\text{He}(2\ ^1P\pi^-)$ (c) initial states.

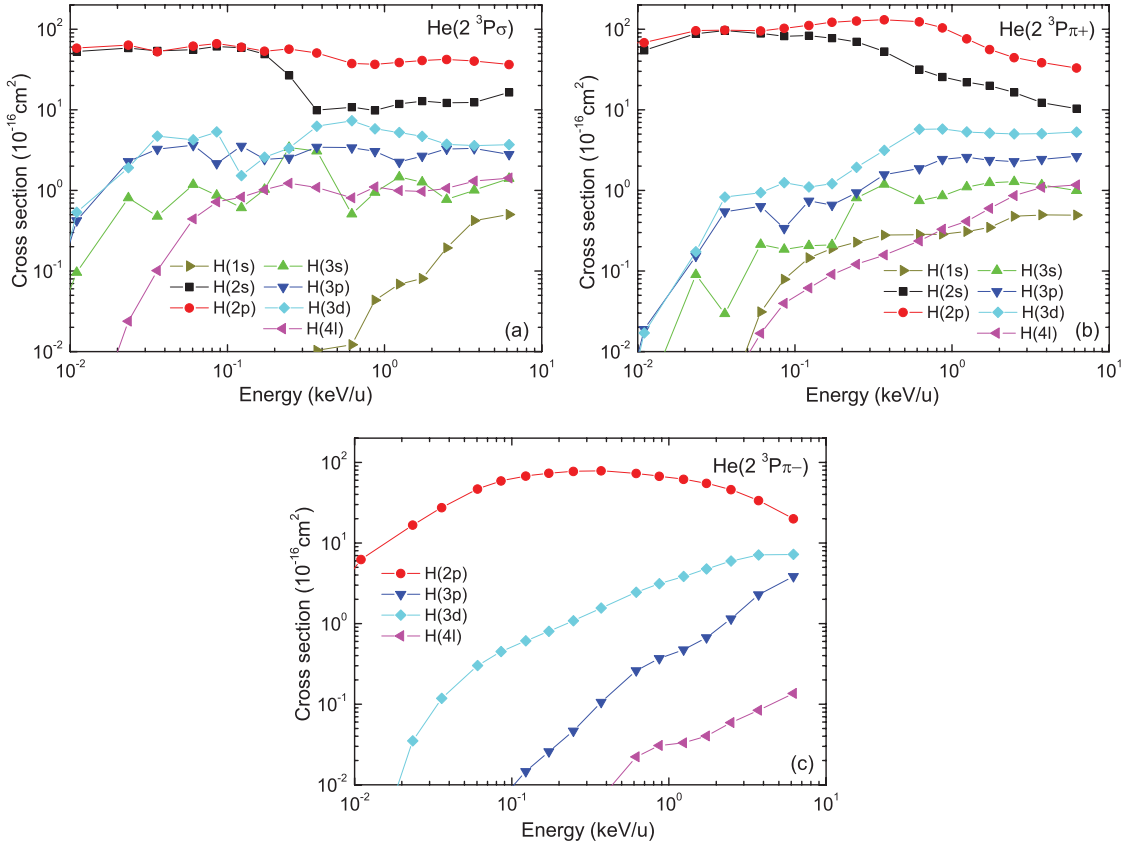


FIG. 12. (Color online) Cross sections for electron capture to $H(n)l$ states from the $\text{He}(2^3P\sigma)$ (a), $\text{He}(2^3P\pi^+)$ (b), and $\text{He}(2^3P\pi^-)$ (c) initial states.

The capture dynamics is reflected in even greater detail in Figs. 11 and 12 where the cross sections for capture to $1s$, $2l$, and $3l$ states and the $n = 4$ shell (denoted by $4l$) are shown for the initial $\text{He}(2^{1,3}P\sigma)$ [panels (a)], $\text{He}(2^{1,3}P\pi^+)$ [panels (b)], and $\text{He}(2^{1,3}P\pi^-)$ [panels (c)] states. For instance, the energy behavior of $2p$ capture cross sections in Figs. 10) and 10(b) in the energy region above ~ 0.5 keV/u are determined mainly by the contributions of reaction paths associated with the $\text{He}(2^{1,3}P\sigma)$ and $\text{He}(2^{1,3}P\pi^+)$ initial states, while below this energy the energy behavior is determined by the exit channels associated with the $\text{He}(2^{1,3}P\pi^-)$ initial states. From Figs. 11(a) and 11(b) and 12(a) and 12(b) it now becomes clear that the main contribution to the capture to the $H(1s)$ state (particularly in the singlet case) gives the rotational $2^1\Pi-2^1\Sigma$ and $1^3\Pi-1^3\Sigma$ couplings.

As we mentioned in the Introduction, the only other calculations performed for the processes (1a) and (1b) in the considered energy range are those in Ref. [6]. The calculations have been made in a basis that uses a Stark representation of the states when centered on H and an angular momentum representation when they are centered on He. The coupling matrix elements between these states have been calculated analytically by using the Landau-Herring asymptotic method [7]. The electron capture amplitudes, obtained by solving the coupled channel equations (with all states having principal quantum numbers $n = 2, 3, 4$ on both centers), have then been projected on angular momentum states of H. As also has been mentioned in the Introduction, neither the rotational couplings nor the ETF effects have been included in the calculations of Ref. [6]. In Table II we give a comparison of the total capture

TABLE II. Total electron capture cross sections for the $\text{He}(2^{1,3}S)$ and $\text{He}(2^{1,3}P)$ initial states.

Energy (keV/u)	Cross sections (10^{-16}cm^2)							
	Chibisov <i>et al.</i> [6]				Present calculation			
	2^1S	2^3S	2^1P	2^3P	2^1S	2^3S	2^1P	2^3P
0.033	16	16	891	61	17	1.7	119	113
0.12	23	12	840	157	63	8.2	116	130
0.65	71	19	821	403	148	38	91	98
1.6	114	12	783	572	127	69	75	70
4.7	204	36	756	621	93	75	73	52

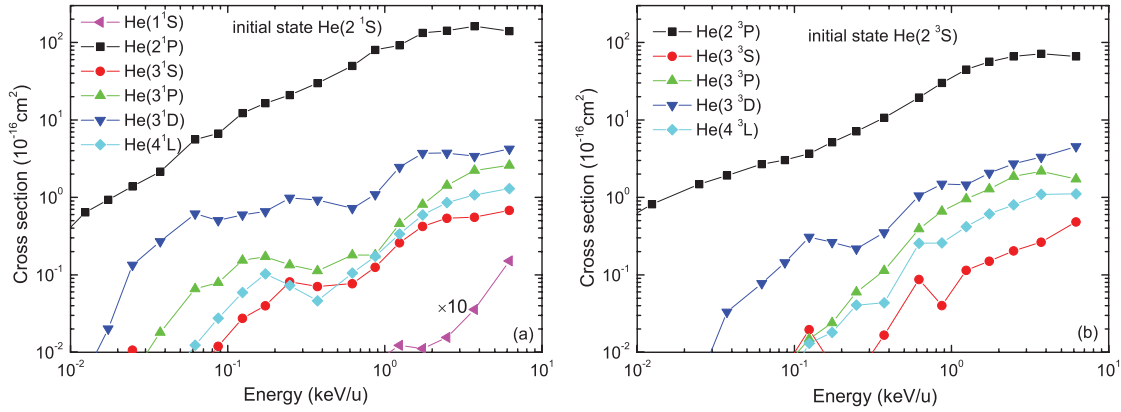


FIG. 13. (Color online) Excitation cross sections to $\text{He}(nl)$ states from the $\text{He}(2\ ^1S)$ (a) and $\text{He}(2\ ^3S)$ initial states. The cross section for deexcitation to $\text{He}(1\ ^1S)$ has been multiplied by 10.

cross sections for the $2\ ^1,3S$ and $2\ ^1,3P$ initial states from the present work and that of Ref. [6] for a number of collision energies. (Shell- or state-selective cross capture cross sections are not given in Ref. [6].) The table shows that the results of Ref. [6] are significantly larger than the present results (except for a few exceptions). This could be a consequence of the large values of radial couplings calculated in Ref. [6] and, most probably, due to the neglected rotational couplings that provide loss channels for the capture probability flux. The neglected ETF effects in Ref. [6] may also contribute to the large cross-section values at energies above a few keV/u. Contrary to the present results, the total capture cross sections for the $2\ ^1,3S$ initial states in Ref. [6] do not show a maximum up to 8.8 keV/u.

B. Excitation cross sections

The collision dynamics leading to the excitation and deexcitation of $\text{He}(n\ ^1,3L')$ ($n = 1,2,3,4$; $L' = S, P, D$) states from a given initial $\text{He}(2\ ^1,3L_m)$ state ($L = S, P$; $m = 0, \pm 1$) is the same as the one discussed in the preceding section for each of the above initial states, except for the different exit channels. Therefore, in the present section we shall focus on some of the specific aspects of excitation and deexcitation channels only.

1. $\text{He}(2\ ^1,3S)$ initial states

The cross section for excitation of $2p$ and $3l$ He states, as well as the l -summed $n = 4$ cross section (denoted as $4L$) from the $\text{He}(2\ ^1S)$ and $\text{He}(2\ ^3S)$ initial states are shown in panels (a) and (b) of Fig. 13, respectively. Also shown in Fig. 13(a) is the deexcitation $2s-1s$ cross section.

Figure 13 shows that for both initial states the cross section for the $2s-2p$ excitation of He is an order (or more) of magnitude larger than those for the excitation of $3l$ and $n = 4$ states. Except in the energy region below ~ 0.05 keV/u, the $2p$ excitation cross section for the $\text{He}(2\ ^1S)$ initial state is larger than the one for the $\text{He}(2\ ^3S)$ initial state. Within the group of $3l$ excitation cross sections, the largest one is that for $3d$ and the smallest one is that for $3s$ for both $\text{He}(2\ ^1S)$ and $\text{He}(2\ ^3S)$ initial states. The energy behavior of $3l$ excitation cross sections exhibit structures similar to those in the $\text{H}(3l)$ capture cross sections (cf. Fig. 8). The reaction paths for each initial state can be analyzed similarly as in the case of electron capture (e.g., using Fig. 6), but the populated final states are now different.

It should be noted that in the case of the $\text{He}(2\ ^3S)$ initial state, the entry channel $2\ ^3\Sigma$ is directly coupled with the $2p\sigma$ ($3\ ^3\Sigma$) exit channel, whereas in the case of the $\text{He}(2\ ^1S)$ initial-state entry ($3\ ^1\Sigma$) and exit $2p\sigma$ ($5\ ^1\Sigma$) channels are coupled indirectly, via the $4\ ^1\Sigma$ [$\text{H}(2s/2p\sigma)$] electron capture

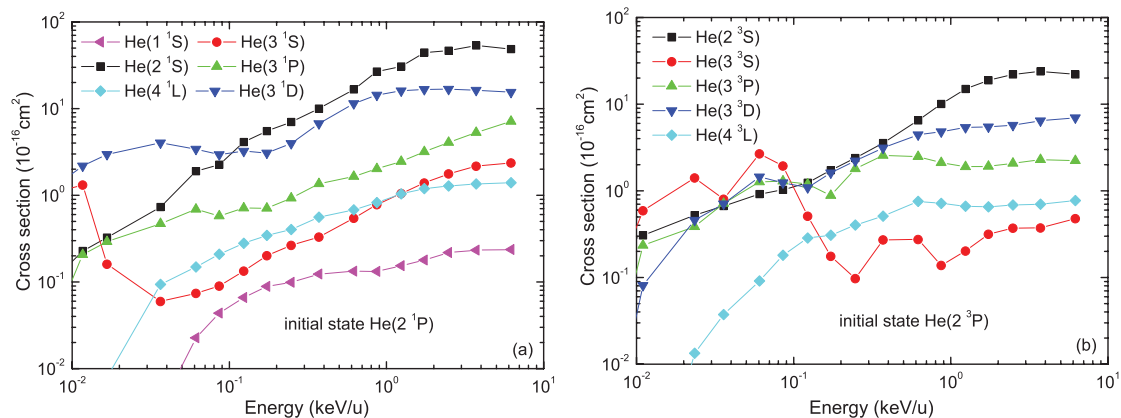


FIG. 14. (Color online) Excitation cross sections to $\text{He}(nl)$ states from the $\text{He}(2\ ^1P)$ and $\text{He}(2\ ^3P)$ initial states.

TABLE III. Total excitation and deexcitation cross sections for the initial He($2^{1,3}S$) and He($2^{1,3}P$) states.

Energy (keV/u)	Cross sections (10^{-16} cm 2)							
	Chibisov <i>et al.</i> [6]				Present calculation			
	2^1S	2^3S	2^1P	2^3P	2^1S	2^3S	2^1P	2^3P
0.033	5.2	3.1			2.3	1.9	5.2	2.9
0.12	45	6.5	23		13	4.0	8.4	4.3
0.65	467	32	162	27	52	21	31	15
1.6	751	136	271	73	137	59	66	27
4.7	1247	452	485	225	159	76	78	33

channel. This circumstance leads to a smaller cross section for excitation of the He($2p\sigma$) substate in the case of the He(2^1S) initial state than in the case of the He(2^3S) initial state, as confirmed by the calculations. On the other hand, since the population of the $2p\pi$ substate for both singlet and triplet initial He($2s$) states is strongly influenced by the $1^1\Pi$ - $2^1\Pi$ and, respectively, $1^3\Pi$ - $2^3\Pi$ coupling, and since the energy difference of the $1^1\Pi$ and $2^1\Pi$ states in the strong-coupling region (≈ 0.602 eV) is significantly smaller than that of the $1^3\Pi$ and $2^3\Pi$ states (≈ 1.144 eV), the cross section for excitation of the $2p\pi$ substate in the case of the He(2^1S) initial state should be considerably larger than that for the case of the He(2^3S) initial state. These two effects account for the difference in the magnitudes of the $2s$ - $2p$ excitation cross sections for the He(2^1S) and He(2^3S) initial states.

2. He($2^{1,3}P$) initial states

The averaged excitation and deexcitation cross sections from the three initial states He($2p\sigma$) and He($2p\pi^\pm$) with singlet and triplet symmetry are shown in panels (a) and (b) of Fig. 14, respectively. The comparison of the cross sections in Figs. 13 and 14 shows significant differences between the excitation and deexcitation for the He($2^{1,3}P$) and He($2^{1,3}S$) initial states. In both singlet and triplet cases, the $2p$ - $2s$ deexcitation cross sections are considerably smaller than the $2s$ - $2p$ excitation cross sections, and the $3l$ excitation cross sections for the He($2^{1,3}P$) initial states are much closer to the $2p$ - $2s$ deexcitation cross sections (particularly in the low energy region, where some of them can be larger than the $2p$ - $2s$ cross section) than are those for the initial He($2^{1,3}S$) initial states close to the $2s$ - $2p$ excitation cross sections. The $2p$ - $1s$ deexcitation cross section is more than an order of magnitude larger than the $2s$ - $1s$ cross section. These differences are partly due the fact that the $2^{1,3}P$ He states are energetically closer to the He($3l$) group of states than are the $2^{1,3}S$ He states and, more importantly, due to differences in the coupling dynamics involved.

In Table III we give a comparison of total excitation plus deexcitation cross sections from the initial He($2^{1,3}S$) and

He($2^{1,3}P$) states of the present results with those of Ref. [6] for a number of collision energies. As in the case of total electron capture cross sections, the results of Ref. [6] are significantly larger than the present ones, particularly at the higher energies. The physical reasons for this disagreement were discussed earlier.

V. CONCLUSIONS

In the present article we have studied the processes of electron capture and excitation in slow collisions of protons with a helium atom in its $2^{1,3}S$ and $2^{1,3}P$ excited states by employing the QMOCC method. For the symmetric states, the expansion basis included all Σ and Π states correlating asymptotically to the $n = 1-4$ H and He atomic states, as well as two Δ states from the $n = 3$ manifold (in total 34 singlet and 33 triplet molecular states), while for the antisymmetric cases, all of the $12^{1,3}\Pi$ and six $1,3\Delta$ states related to the $n = 2-4$ H and He atomic states are considered. The collision dynamics was discussed in terms of the most important reaction paths and the involved radial and rotational couplings leading to final angular momentum nl projectile (electron capture) or target (excitation) states with $n = 1-3$. The nl -selective ($n = 1-3$) and n -shell ($n = 1-4$) cross sections for electron capture and excitation have been calculated in the energy range 0.01–6 keV/u. The comparison of present results for the total excitation and electron capture cross sections with those of Ref. [6] shows that the rotational couplings play a critical role in the collision dynamics and, consequently, in determining the magnitude and energy behavior of both the excitation and electron capture cross sections.

ACKNOWLEDGMENTS

This work was supported by the International Atomic Energy Agency (Vienna, Austria) (Research Contracts No. 15689/R0 with R.K.J. and No. 15700/R0 with J.G.W.) and by the National Natural Science Foundation of China (Grants No. 11004014, No. 11025417, and No. 10974021).

- [1] R. K. Janev (ed.), *Atomic and Plasma-Material Interaction Data for Fusion* (Supplement to the J. Nuclear Fusion), Vol. 3 (International Atomic Energy Agency, Vienna, 1992).
 [2] A. I. Kislyakov, V. I. Afanassiev, A. V. Khudoleev, S. S. Kozlovskii, and M. P. Petrov, *Diagnostics for Experimental*

Thermonuclear Fusion Reactors (Plenum, New York, 1998), p. 353.

- [3] A. A. Korotkov and R. K. Janev, *Phys. Plasmas* **3**, 1512 (1996).
 [4] W. Fritsch, *Phys. Lett. A* **158**, 227 (1991).
 [5] A. Igarashi and T. Shirai, *Phys. Scr. T* **62**, 95 (1996).

- [6] M. I. Chibisov, R. K. Janev, X. Urbain, and F. Brouillard, *J. Phys. B* **35**, 5081 (2002).
- [7] M. I. Chibisov, R. K. Janev, X. Urbain, and F. Brouillard, *J. Phys. B* **34**, 2631 (2001).
- [8] R. J. Buenker and R. A. Phillips, *J. Mol. Struct.: THEOCHEM* **123**, 291 (1985).
- [9] S. Krebs and R. J. Buenker, *J. Chem. Phys.* **103**, 5613 (1995).
- [10] B. H. Bransden and M. R. C. McDowell, *Charge Exchange and the Theory of Ion-Atom Collisions* (Clarendon, Oxford, 1992).
- [11] B. Zygelman, D. L. Cooper, M. J. Ford, A. Dalgarno, J. Gerratt, and M. Raimondi, *Phys. Rev. A* **46**, 3846 (1992).
- [12] B. R. Johnson, *J. Comput. Phys.* **13**, 445 (1973).
- [13] M. C. Bacchus-Montabonel and P. Ceyzeriat, *Phys. Rev. A* **58**, 1162 (1998).
- [14] L.F. Errea, L. Mendez, and A. Riera, *J. Phys. B* **15**, 101 (1982).
- [15] T. G. Heil, S. E. Butler, and A. Dalgarno, *Phys. Rev. A* **23**, 1100 (1981).
- [16] T. H. Dunning Jr., *J. Chem. Phys.* **90**, 1007 (1989).
- [17] G. Hirsch, P. J. Bruna, R. J. Buenker, and S. D. Peyerimhoff, *Chem. Phys.* **45**, 335 (1980).